Deep reinforcement transfer learning of active control for bluff body flows at high Reynolds number

Zhicheng Wang[1,3]† Dixia Fan [2] † Xiaomo Jiang[3,4] Michael S. Triantafyllou[5,6] † and George Em Karniadakis[7]

[1]Laboratory of Ocean Energy Utilization of Ministry of Education, Dalian University of Technology, Dalian, 116024, China

[2]School of Engineering, Westlake University, Hangzhou, 310024, China

[3]State Key Lab of Structural Analysis, Optimization and CAE Software for Industrial Equipment, Provincial Key Lab of Digital Twin for Industrial Equipment, Dalian University of Technology, Dalian, 116024, China

[4]School of Energy and Power Engineering, Dalian University of Technology, Dalian, 116024, China

[5]Department of Mechanical Engineering, Massachusetts Institute Technology, Cambridge, MA 02139, USA

[6]MIT Sea Grant College Program, Cambridge, MA, 02139, USA

[7]Division of Applied Mathematics and School of Engineering, Brown University, Providence, RI 02912 USA

(Received xx; revised xx; accepted xx)

We demonstrate how to accelerate the computationally taxing process of deep reinforcement learning (DRL) in numerical simulations for active control of bluff body flows at high Reynolds number (Re) using transfer learning. We consider the canonical flow past a circular cylinder whose wake is controlled by two small rotating cylinders. We first pre-train the DRL agent using data from inexpensive simulations at low Re, and subsequently we train the agent with small data from the simulation at high Re (up to $Re = 1.4 \times 10^5$). We apply transfer learning (TL) to three different tasks, the results of which show that TL can greatly reduce the training episodes, while the control method selected by TL is more stable compared to training DRL from scratch. We analyze for the first time the wake flow at $Re = 1.4 \times 10^5$ in detail and discover that the hydrodynamic forces on the two rotating control cylinders are not symmetric.

Key words: Deep reinforcement learning, bluff body, drag reduction, high Reynolds number

1. Introduction

Deep reinforcement learning (DRL) has been shown to be an effective way of selecting optimal control of flows in diverse applications, including fish bio-locomotion (Gazzola *et al.* 2014; Verma *et al.* 2018), optimization of aerial/aquatic vehicles' path and motion (Reddy *et al.* 2016; Colabrese *et al.* 2017; Novati *et al.* 2019), active flow control for bluff bodies (Ma *et al.* 2018; Bucci *et al.* 2019; Rabault *et al.* 2019; Ren *et al.* 2021), shape optimization (Viquerat *et al.* 2021), and learning turbulent wall models (Bae & Koumoutsakos 2022).

The flow past a smooth circular cylinder has been characterized as a "kaleidoscope" (Morkovin

† Email address for correspondence: mistetri@mit.edu

1964) of interesting fluid mechanics phenomena as the Reynolds number ($Re_D = \frac{UD}{\nu}$) is increases from 20 to 2×10^5 (Cheng *et al.* 2017; Dong *et al.* 2006). The flow develops from two-dimensional steady wake to three-dimensional unsteady vortex shedding, followed by wake transition, shear layer instability, and boundary layer transition. Due to the large contrast among flow patterns of different scales, accurate numerical simulations of turbulent flow are usually limited to small and moderate Re_D. For the same reason, using numerical simulation to study active control of the flow at high Re_D has rarely been reported.

In our previous study (Fan *et al.* 2020), an efficient DRL algorithm was developed to discover the best strategy to reduce the drag force, by using the DRL to control the rotation of two small cylinders placed symmetrically in the wake of the big cylinder. Specifically, for the flow at $Re_D = 10^4$, it has been demonstrated that DRL can discover the same control strategy as experiments in learning from data generated by the high fidelity numerical simulation. Simulated data is noise free, but learning from the simulated data is restricted by the simulation speed. For instance, in (Fan *et al.* 2020), in the case of $Re_D = 10^4$, it took 3.3 hours to generate the simulated data for each episode, and one month to finalize the DRL strategy. In contrast, in companion experimental work it only took a few minutes to learn the same control strategy. As Re_D increases to 1.4×10^5, one can expect that even for the simplest task in (Fan *et al.* 2020), performing DRL from scratch could take months, and hence it might not be practical to apply DRL directly to the more difficult tasks at higher Re_D.

In this paper, in order to tackle the aforementioned problem, we propose a learning paradigm that first trains the DRL agent using the simulated data at low Re_D and subsequently transfers the domain knowledge to the learning at higher Re_D. The rest of the paper is organized as follows: section 2 gives the details of the simulation model, numerical method and DRL algorithm; section 3 presents the DRL and transfer learning results for different tasks at three different Re_D, namely, $Re_D = 500$, $Re_D = 10^4$ and $Re_D = 1.4 \times 10^5$; section 4 gives the conclusion of the current paper. Finally, appendix A presents the simulation results of the cases that the control cylinders are rotating at constant speed, while appendix B presents the validation of the numerical method for simulations at high Reynolds number.

2. Model and Methods

In this paper, the bluff body flow control problem has the same geometry as the one in (Fan *et al.* 2020) but here we focus on demonstrating the feasibility of transferring DRL knowledge from low Re_D to high Re_D, solely in the environment of numerical simulation. As shown in Fig. 1, the computational model consists of a main cylinder and two fast rotating smaller control cylinders. This configuration is used to alter the flow pattern around the wake of the big cylinder, with the objective of reducing the effective system drag, or maximizing the system power gain. We note that a similar control strategy has been been studied at low Reynolds number and has been shown that when the control cylinders are placed at appropriate locations and rotating at a sufficiently fast speed, they are able to change the boundary layers on the main cylinder, i.e., reattach the boundary layer and form a narrower wake, resulting in notable drag reduction.

2.1. *Numerical method*

The numerical simulation of the unsteady incompressible flow past the cylinders of different diameters is achieved by employing the high-order CFD code *Nektar* that employs spectral element discretization on the $(x - y)$ plane and Fourier expansion along the cylinder axial direction (z) (Karniadakis & Sherwin 2005). In particular, we employ the entropy viscosity method (EVM) based large-eddy simulations (LES), which was originally proposed by (Guermond *et al.* 2011*a*,*b*) and later developed further for complex flows by (Wang *et al.* 2019, 2018). In the simulations, the

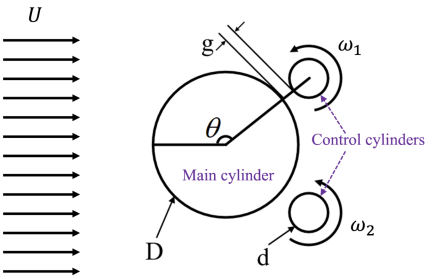

Figure 1: Sketch of the flow control problem. U is the inflow velocity, D is the diameter of the main cylinder, $d = \frac{1}{8}D$ is the diameter of the control cylinder, $g = \frac{1}{20}D$, $\theta = 120^o$. ω_1, ω_2 are the angular velocities of the control cylinder 1 and 2, respectively. Specifically, $\omega_1 = \epsilon_1\, \epsilon_{\max}$, $\omega_2 = \epsilon_2\, \epsilon_{\max}$, where ϵ_1 and $\epsilon_2 \in [0, 1]$ are given by the DRL agent, and $\epsilon_{\max}$ is a constant.

computational domain has a size of $[-7.5\,D, 20\,D]\times[-10\,D, 10\,D]$ in x, y direction, respectively. A uniform inflow boundary condition ($u = U$, $v = 0$, $w = 0$) is prescribed at $x = -7.5\,D$, where u, v, w are the three components of the velocity vector $\mathbf{u}$. The outflow boundary ($\frac{\partial \mathbf{u}}{\partial \mathbf{n}} = 0$ and $p = 0$) is imposed on $x = 20\,D$, where p is the pressure, and $\mathbf{n}$ is the normal vector. Wall boundary condition is applied on the main cylinder surface, while the velocity on the control cylinders are given by the DRL agent during the simulation. Moreover, a periodic boundary condition is assumed on the lateral boundaries ($y = \pm 10\,D$). Note that the spanwise length of the computational domain depends on the Re_D, namely, it is $6\,D$ and $2\,D$ in the simulation of $Re_D = 10^4$ and $Re_D = 1.4 \times 10^5$, respectively.

The computational mesh is similar to the one used in (Fan *et al.* 2020). At $Re_D = 500$, the computational domain is partitioned into 2 462 quadrilateral elements, while at $Re_D = 10^4$ and $Re_D = 1.4 \times 10^5$, it consists of 2 790 quadrilateral elements. The elements are clustered around the cylinders in order to resolve the boundary layers. Specifically, on the main cylinder wall normal directions, the size of the first layer element (Δr) is designed carefully so that at $Re = 10^4$, $\Delta r = 4 \times 10^-3$; at $Re_D = 1.4 \times 10^5$, $\Delta r = 1.6 \times 10^{-3}\, D$. On this mesh, with the spectral element mode 4, $y^+ < 1$ can be guaranteed. In the simulation, the time step (Δt) satisfies the Courant condition CFL $= \frac{\Delta t\, |u|}{\Delta x} \leqslant 0.75$. Note that in all the DRL cases the time duration between two consecutive state queries is fixed at $0.12\frac{D}{U}$, e.g., in the case of $Re_D = 1.4 \times 10^5$, $\Delta t = 10^{-4}$, the state data will be collected every 1 200 steps. It is worth noting that the RL guided LES starts from the fully turbulent flow, which is the result of previous simulation of flow in the same geometry configuration with the small cylinders held still.

2.2. *Deep reinforcement learning and transfer learning*

DRL identifies the optimal control strategy by maximizing the expected cumulative reward, using the data generated by the simulation. More details of the DRL can be seen in (Fan *et al.* 2020), but the main principle is summarized as follows,

$$J(\pi) = \mathbb{E}_{(s_i, a_i)\sim p_\pi} \sum_{i=0}^{T} \gamma^i r_i, \tag{2.1}$$

where J is the called cumulative reward, $\mathbb{E}$ denotes the calculation of the expected value, $\gamma \in (0, 1]$ is a discount factor and p_π denotes the state-action marginals of the trajectory distribution induced by the policy π. $s_i \in \mathcal{S}$ is the observed state, $a_i \in \mathcal{A}$ is the given actions with respect to the policy $\pi : \mathcal{S} \rightarrow \mathcal{A}$, and r_i is the received reward, at discrete time step i. As shown in Equation 2.1, the

objective of DRL is to discover the policy π_ϕ parameterized by ϕ, which maximizes the expected cumulative reward. Specifically, in the current work, the state variable is the concatenation of C_L, C_D, $C_{f,1}$ and $C_{f,2}$, the action is the concatenation of ϵ_1 and ϵ_2, where C_D and C_L are the drag and lift force coefficient, $C_{f,1}$ and $C_{f,2}$ are the frictional force coefficient on the control cylinder 1 and 2, ϵ_1 and ϵ_2 are the action variable for control cylinder 1 and 2, respectively.

In this paper, the Twin Delayed Deep Deterministic Policy Gradient Algorithm (TD3) (Fujimoto *et al.* 2018; Fan *et al.* 2020) has been employed. TD3 consists of two neural networks, one for the actor and the other one for the critic, and both are feedforward neural networks with two hidden layers and 256 neurons. The discount factor γ is set as 0.99. The standard deviation of the policy exploration noise σ is set as 0.005. The Adam optimizer with learning rate 10^{-4} is used, and the batch size is $N = 256$.

Before proceeding to the results, it is worthy discussing the difficulties of training the model-free DRL feeding with simulated data. The first difficulty is how to generate more training data as fast as possible. To this end, this paper will propose a multi-client-mono-server DRL paradigm, in which multiple simulations running simultaneously and independently to provide training data to the single DRL server. In each simulation, once a training data is collected, it will be provided to the DRL server. Note that, the data exchange between the DRL server and simulation clients is achieved by the XML-RPC protocol.

The second difficulty concerns the simulation at high Reynolds number, which makes the multi-client-mono-serve DRL not practical, since a single simulation already requires a significant amount of computing resource. To overcome this difficulty, initially, the DRL agent will be trained using the data collected from the much cheaper simulations at low Re_D, and then the neural networks will be used in the simulation at high Re_D, while the network parameters will be re-trained using the new data.

3. Results and discussion

In order to demonstrate the feasibility of using TL in DRL for active flow control, we consider three different tasks, in which the states, actions, and reward functions, corresponding to each task, are given as follows,

- **Task 1:** Minimizing C_D: two states, C_D and C_L; two independent actions, ϵ_1 and ϵ_2; reward function, $r = -sign(C_D)C_D^2 - 0.1C_L^2$.
- **Task 2:** Maximization of the system power gain efficiency: four states, C_D, C_L, $C_{f,1}$ and $C_{f,2}$; one action, $\epsilon_1 = -\epsilon_2$; reward function $r = -\eta$, where

$$\eta = |C_D| + \frac{\pi d}{D}\left(|\epsilon_1|^3 C_{f,1} + |\epsilon_2|^3 C_{f,2}\right)\epsilon_{\max}^3. \tag{3.1}$$

- **Task 3:** Maximization of the system power gain efficiency: sates and reward functions are the same as those in **Task 2**; two independent actions, ϵ_1 and ϵ_2.

3.1. *Learning from scratch at low Re*

We start DRL for **Task 1** from scratch with $\epsilon_{max} = 5$, in three dimensional simulation of flow at $Re_D = 500$. Before presenting the results, we explain why $\epsilon_{max} = 5$ is chosen. As shown in our previous study (Fan *et al.* 2020), $\overline{C_D}$ decreases with ϵ_{max}, which implies that the generated state variables (C_D, C_L) will be located in a wider range with increasing ϵ_{max}. In order to enhance the generalization of the neural networks, it is beneficial to experience the training data in a wider range before transferring to a more challenging task.

Fig. 2 shows the evolution of ϵ_1, ϵ_2, C_D and C_L, as well as the variation of the vortex shedding pattern due to active control by DRL at $Re_D = 500$. Initially for (40 episodes approximately), DRL knows very little on how to minimize C_D; small values of ϵ_1, ϵ_2 are provided by DRL, thus

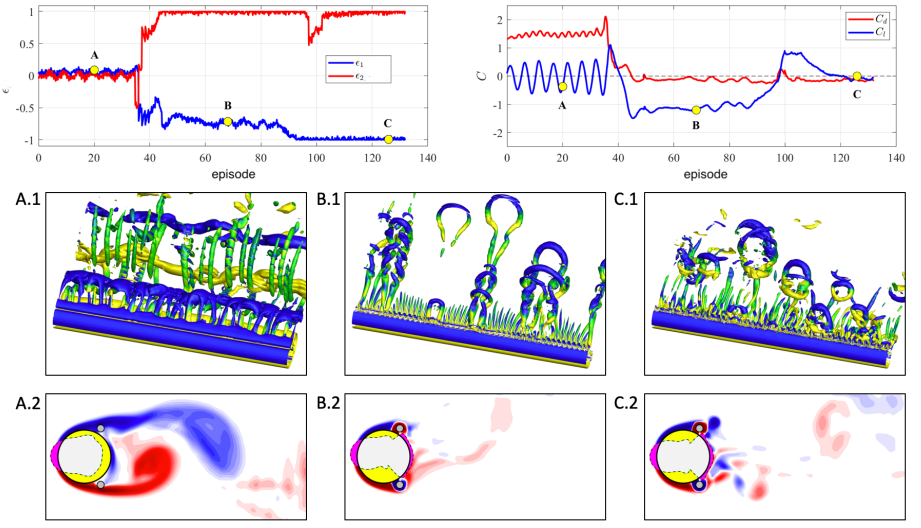

Figure 2: Task 1: Evolution of reinforcement learning and corresponding simulated three-dimensional vortex shedding patterns at $Re_D = 500$, $\epsilon_{\max} = 5$. Note that the DRL is starting from scratch, but the simulation is starting from a fully developed flow where the smaller controlling cylinders are stationary.

the control cylinders have small effect on the flow, hence regular vortex shedding pattern can be observed, as shown by figure A.1 and A.2. However, around the 40$^{\text{th}}$ episode, DRL has figured out the correct rotating direction to reduce C_D, and the wake patterns are now hairpin vortices emanating from the gap between the control and main cylinder. At this stage, $\epsilon_1 \neq \epsilon_2$, and the wake behind the main cylinder is not symmetric, which gives rise to a large C_L, as shown in sub-figures B.1 and B.2. Around 110$^{\text{th}}$ episode, DRL finally identified the best rotation speed to minimize C_D, and, correspondingly, the vortex shedding from the main cylinder has been eliminated.

To sum up, when DRL networks are initialized randomly, the DRL agent can gradually manage to learn the optimal policy. The learning process has lasted for more than 100 episodes, and the generated training data, C_D and C_L, are roughly in the ranges $[-0.1, 2.0]$ and $[-1.5, 1.0]$, respectively.

3.2. *Transfer learning from low Re to high Re*

In the previous subsection, we have demonstrated that for the flow at low Reynolds number, although the training data from the simulation are noise free, it still takes DRL to go through 100 episodes, i.e., 1000 data points, to discover the right policy. Hence, DRL from scratch is impractical to be applied to flow at high Re, since it will tax the computational resources heavily, as it will take much longer to generate the training data. In order to use the data more efficiently and reduce the overall computing time, we employ a transfer learning approach at high Re_D.

Fig. 3 presents the time traces of ϵ_1, ϵ_2 and C_D of **Task 1** with $\epsilon_{max} = 3.66$ at $Re_D = 10^4$ and $Re_D = 1.4 \times 10^5$. In particular, the results of DRL from scratch at $Re_D = 10^4$ are plotted together. Note that here both cases of TL were initialized using the same DRL network, which was obtained in **Task 1** at $Re_D = 500$ shown in Fig. 2(a). We observe that TL spent 60 episodes only to discover the optimal policy, while the DRL from scratch went through over 200 episodes to reach a comparable decision. Moreover, ϵ_1 (pink line, in sub-figure(a)) given by the DRL from scratch keeps oscillating even after 500 episodes, but the value given by the TL shows less variation, although the same value of the noise parameter (σ) is used in both cases.

In particular, in the TL at $Re_D = 10^4$, as shown in Figure 3, the TL agent manages to find the correct rotating direction in less than 10 episodes, and as it reaches 20^{th} episodes, the TL starts exploring a new policy, during which both ϵ and C_D show notable variations, associated with the so-called "catastrophic forgetting" (Kirkpatrick *et al.* 2017). After 55^{th} episode, the TL can make the correct and stable decision.

In **Task 1**, as Re_D is increased from 10^4 to 1.4×10^5, the wake behind the main cylinder becomes very complex, although the boundary layer is laminar at both values of Re_D. The learning process at $Re_D = 1.4 \times 10^5$ is very similar to that of $Re_D = 10^4$. In 25 episodes, the TL is able to identify the correct rotating directions. At 50^{th} episode, the rotating speed on the control cylinder 1 begins to show variation and and it starts a new exploration, due to the catastrophic forgetting. Around 80^{th} episode, the rotating speed on the control cylinder 2 also starts to vary, but the rotating speeds on both control cylinders quickly return to optimal value, i.e., $|\epsilon_{\pm 1}| = 1$.

We would like to emphasize that the high fidelity large-eddy simulation of flow past a cylinder accompanied by two rotating cylinders at $Re_D = 1.4 \times 10^5$ is still a challenge. To the best of the authors' knowledge, the details of the flow pattern have not been studied before. In figure 3 (d), the top snapshot exhibits the vortical flow, while the control cylinders remain stationary. The bottom snapshot shows the flow structures at 125^{th} episode, when the control cylinders are rotating at optimal speed. We see that as the control cylinder is rotating, the large scale streamwise braid vortices are mostly replaced by the hairpin vortices emanating from the gap between the main cylinder and control cylinders, and the wake becomes narrower, which is a sign of a smaller C_D.

Next we turn our attention to Task 2, where the objective is to maximize the system power gain efficiency, η, under the condition that $\epsilon_2 = -\epsilon_1$. Note that the objective of the current **Task 2** is similar to the **Task 2** in our previous study (Fan *et al.* 2020), except that here we have used the instantaneous C_f obtained from the simulation, while C_f is a pre-defined constant in (Fan *et al.* 2020). Nonetheless, our previous study has revealed that it is much more difficult for DRL to identify the optimal control strategy in **Task 2** than that in **Task 1**. In **Task 2**, we have started from the DRL from scratch using two dimensional (2D) simulation at $Re_D = 500$. In particular, since the 2D simulation is relatively inexpensive and fast, we have run 16 simulations concurrently to provide the training data to a single DRL. For the TL at $Re_D = 10^4$ and $Re_D = 1.4 \times 10^5$, the simulation is very expensive, thus only a single simulation was performed. It is worthy noting that η at low Re_D is very different from that at high Re_D, as shown in Appendix A, thus it is expected that TL in **Task 2** and **Task 3** will be more challenging.

Figure 4(a) shows the learning process of DRL from scratch for **Task 2** at $Re_D = 500$. In particular, the learning process using a single 2D simulation (left part) and 16 2D simulations (right) are plotted together. In the left part of figure 4(a), DRL manages to find the correct rotating direction after 75 episodes, but it barely makes the optimal decision, although it has been trained over 300 episodes. On the other hand, in the case of 16 simulations running concurrently, as shown in the right part of figure 4(a), DRL can identify the correct rotating direction in less than 10 episodes, and is able to make the optimal decision before the 75^{th} episode.

Subsequently, the DRL networks trained in figure 4 (a) are both applied to the TL at $Re_D = 10^4$, and the results are shown in figure 4(b). We observe from the left part of figure 4(b) that although the DRL of figure (a) has identified the correct policy it gives a very chaotic ϵ_1 in the first 60 episodes in TL. On the other hand, as shown in right part of figure 4(b), the TL is able to give the correct rotating direction in less than 10 episodes, and after 30 episodes it has managed to reach the optimal decision. When applied to the simulation flow at $Re = 1.4 \times 10^5$, the TL manages to give stable action values after the 30^{th} episode, but in short period just after the 40^{th} episode and until the end of the simulation, an unstable action is given as shown by the variation of ϵ_1 and η in the left part of figure 4(c). To explain the variation of the decision given by the agent, the policy at 5^{th}, 15^{th}, 25^{th} and 65^{th} episodes are visualized in the right part of figure 4 (c). Specifically,

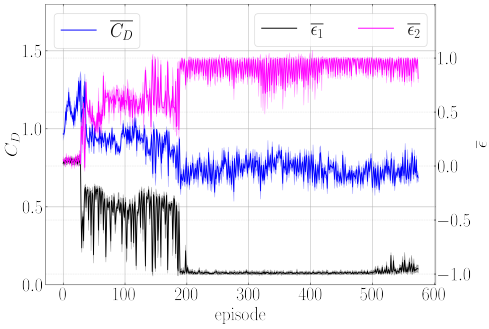

(a) Learning from scratch, $Re_D = 10^4$.

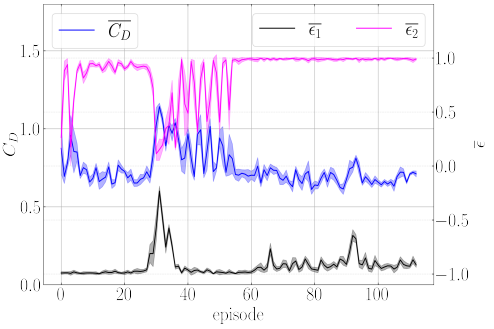

(b) Transfer learning, $Re_D = 10^4$.

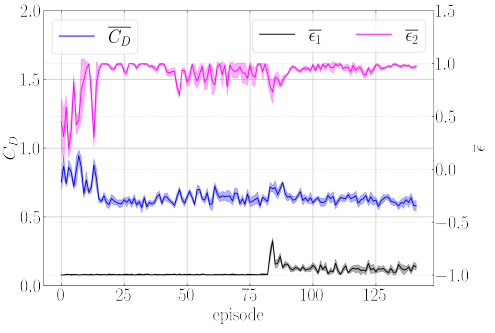

(c) Transfer learning, $Re_D = 1.4 \times 10^5$

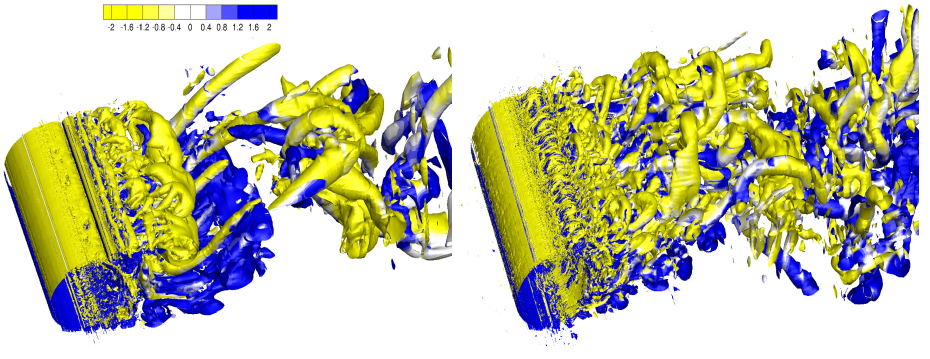

(d) Wake pattern, $Re_D = 1.4 \times 10^5$

Figure 3: **Task I**: Comparison between DRL from scratch and transfer learning at different Re. Figure (a) - learning from scratch at $Re_D = 10^4$; figure (b) - transfer learning $Re_D = 10^4$; figure (c) - transfer learning at $Re_D = 1.4 \times 10^5$; figure (d) - vortex shedding pattern, the control cylinders are stationary (upper figure), and the pattern at 125$^{\text{th}}$ episode (lower figure). Note that in Figures (a),(b) and (c), the pink and black lines are the time traces of actions (($\overline{\epsilon}/\epsilon^{max}$, where $\epsilon_{max} = 3.66$) on control cylinder 1 and 2. Blue line is the time trace of C_D. The agent of the transfer learning was initialized from the saved agent in the previous case at $Re_D = 500$, as shown in figure 2.

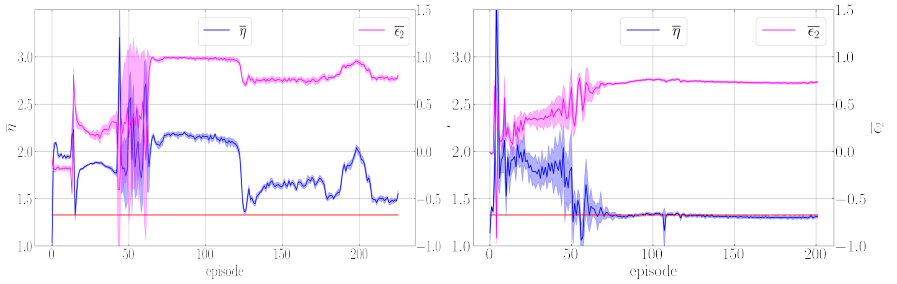

(a) Learning from scratch, $Re_D = 500$.

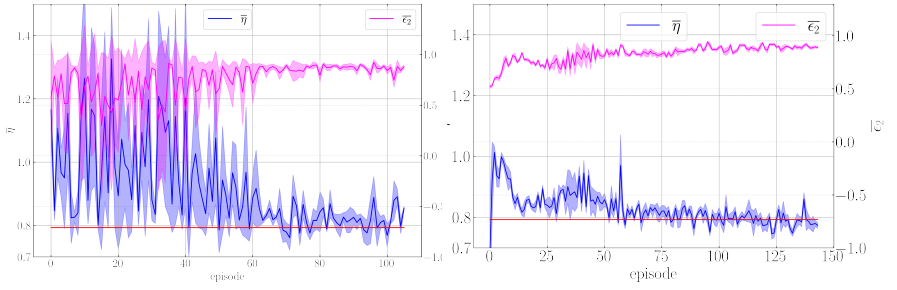

(b) Transfer learning, $Re_D = 10^4$.

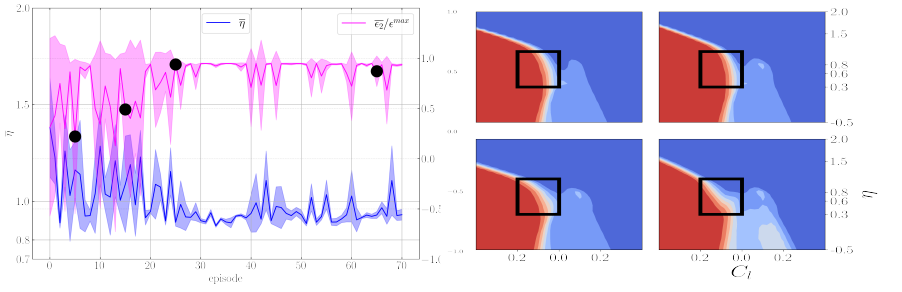

(c) Transfer learning, $Re_D = 1.4 \times 10^5$.

Figure 4: **Task 2:** Transfer learning from 2D low Re_D to 3D high Re_D. Figure (a) - learning from scratch, $Re_D = 500$: left one - single-client; right one - multi-client. Figure (b) - transfer learning, $Re_D = 10^4$: the left and right ones are initialized by the corresponding DRL agents shown in the left and right part of figure (a), respectively. Figure (c) - transfer learning, $Re_D = 1.4 \times 10^5$, initialized from the agent corresponding to right part of figure (b). Right panel of figure (c) - visualization of the policy at 5$^{\text{th}}$, 15$^{\text{th}}$, 25$^{\text{th}}$ and 65$^{\text{th}}$ episode. Note in all the simulations here $\epsilon_{max} = 3.66$.

the black boxes $[-0.25, 0.25] \times [0.3, 0.8]$, which correspond to the concentrated intervals of C_L and C_D, respectively, are highlighted. We observe that the policy in the highlighted regions has not reached the best strategy yet, although the TL has been trained for 70 episodes. Next we consider the hardest problem of this paper, **Task 3**, with the same objective as that of **Task 1**, but ϵ_1 and ϵ_2 are independent. Again, we start this task from scratch in 2D simulation at $Re_D = 500$, as shown in figure 5(a). Note that here 16 2D simulations were used to provide training data. As shown in figure 5(a), the RL agent was able to give correct rotating directions for both controlling cylinders after 50 episodes. Between 50$^{\text{th}}$ and 110$^{\text{th}}$ episodes, ϵ_2 gradually approaches to -1, while ϵ_1 oscillates around 0.7, the combination of which gives rise to $\eta \approx 1.5$. After 110$^{\text{th}}$ episode, the DRL suddenly changes its actions, in a short period of exploration: ϵ_1 changes to 1, ϵ_2 is -0.5, and the value of η goes down to 1.37. Meanwhile, the DRL does not stop exploration on ϵ_1, as

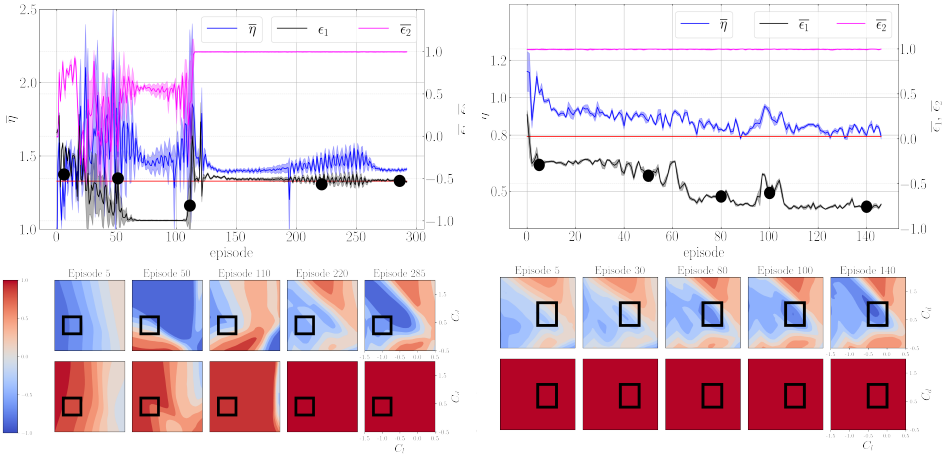

(a) Learning from scratch, $Re_D = 500$

(b) Transfer learning, $Re_D = 10^4$

Figure 5: **Task 3:** ϵ_1 and ϵ_2 are independent. Figure (a), DRL from scratch using 16 2D simulations at $Re_D = 500$; figure (b), transfer learning at $Re_D = 10^4$. Lower panel of the figure, where top row refers to ϵ_1 and the bottom row refers to ϵ_2, shows the policy at the episodes indicated by the black circles in the corresponding figure of upper panel, respectively.

shown by the variation in the black line, starting around 200$^{\text{th}}$ episode. Around 280$^{\text{th}}$ episode, the DRL is able to reach a near optimal decision, as demonstrated by the fact that η is close to 1.325, which is the optimal value obtained from **Task 2**.

The transfer learning results of **Task 3** at $Re_D = 10^4$ are plotted in figure 5(b). We observe that TL is able to reach the correct decision on rotating directions in less than 10 episodes. As more training data is obtained, ϵ_2 keeps the maximum value 1, and ϵ_1 is gradually increased to around $\epsilon_1 = -0.8$, which gives rise to $\eta \approx 0.84$ that is slightly greater than the optimal value $\eta = 0.78$, obtained in **Task 2**. The policy contour at 5$^{\text{th}}$, 50$^{\text{th}}$, 110$^{\text{th}}$, 220$^{\text{th}}$ and 285$^{\text{th}}$ episode for $Re_D = 500$ and 5$^{\text{th}}$, 30$^{\text{th}}$, 80$^{\text{th}}$, 100$^{\text{th}}$ and 140$^{\text{th}}$ episode for $Re_D = 10^4$ are plotted on the bottom part of figure 5(a) and (b), respectively. During the learning process, at $Re_D = 500$, C_D and C_L are mostly in the range $[0.1, 0.6]$ and $[-1.25, -0.75]$, and at $Re_D = 10^4$, these two coefficients are mostly in the range $[0.3, 0.8]$ and $[-0.5, 0.0]$, respectively. The corresponding C_D, C_L ranges are highlighted by black boxes in the two figures. We observe that at both Re_D, the policies for ϵ_1 and ϵ_2 both gradually approach the value that results in optimal η, which clearly shows the exploration and exploitation stages at work.

4. Summary

We have implemented a deep reinforcement learning (DRL) in the numerical simulation of bluff body flow active control at high Reynolds number ($Re_D = 1.4 \times 10^5$). We demonstrated that by training the DRL using the simulation data at low Re_D, and then apply transfer learning at high Re_D, the overall learning process can be accelerated substantially. In addition, the study shows that the transfer learning can result in more stable decision, which is potentially beneficial to the flow control. Moreover, we proposed a multi-clients-single-server DRL paradigm that is able to generate training data much faster to quickly discover an optimal policy. While here we focus on a specific external flow, we believe that similar conclusions are valid for wall-bounded flows and different control strategies.

270

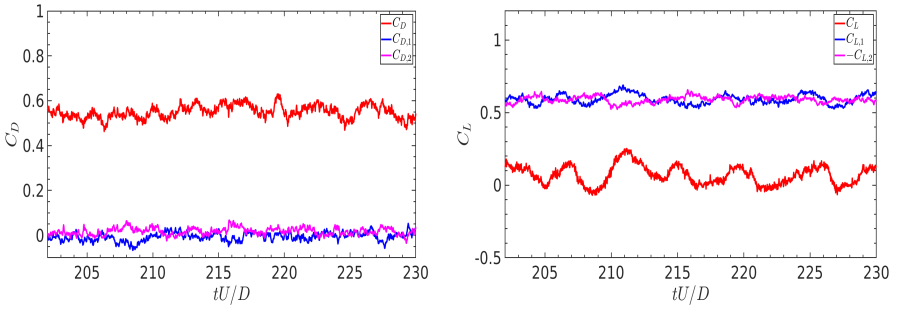

(a) $Re_D = 10^4$.

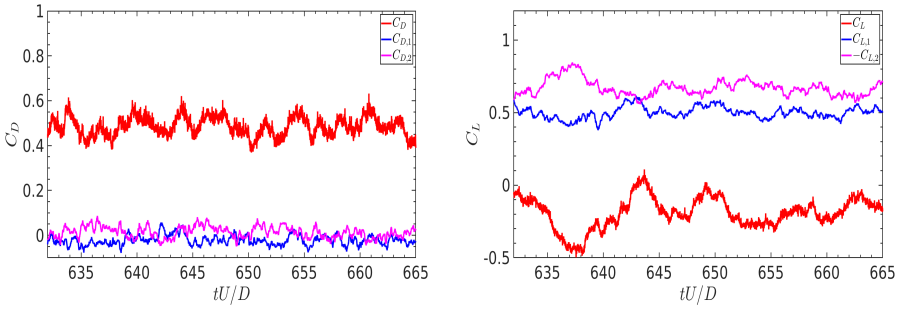

(b) $Re_D = 1.4 \times 10^5$.

Figure 6: Time series of C_D and C_L on the main and control cylinders: figure(a), $Re_D = 10^4$; figure(b), $Re_D = 1.4 \times 10^5$. Note that the control cylinders are rotating at constant speed at $\epsilon_1 = -1$, $\epsilon_2 = 1$, $\epsilon_{\text{max=3.66}}$. The red lines are the the hydrodynamic force coefficients on the main cylinder, while the blue and pink ones are on the control cylinder 1 and 2, respectively.

Appendix A. Simulation results of control cylinders rotating at constant speed

In this section, the simulation results for the cases that both control cylinders are rotating at constant speed $|\Omega| = \epsilon_{\text{max}} = 3.66$. Figure 6 (a) and figure 6(b) show C_D and C_L on the three cylinders at $Re_D = 10^4$ and $Re_D = 1.4 \times 10^5$, respectively. We observe that with rotating control cylinders, the C_D on the main cylinder at both Re_D is reduced significantly. With $\epsilon_{\text{max}} = 3.66$, the control cylinders are not able to cancel the vortex shedding on the main cylinder, thus the C_L on the main cylinder at both Re_D exhibits the frequency of vortex shedding. In particular, at $Re_D = 1.4 \times 10^5$, the magnitude of C_L on the control cylinder 1 and 2 shows notable discrepancy with each other, which leads to symmetry breaking on the average at this Re_D. In addition, figure 7 plots the C_f on the control cylinders at both Re_D. As shown in the figure, at both Re_D, on average, the magnitude of C_f on the control cylinders are different.

In order to validate the optimal control strategy given by DRL in **Task 2** and **Task 3**, additional simulations with $\epsilon_2 = 0$, $\epsilon_2 = 0.6$, $\epsilon_2 = 0.75$, $\epsilon_2 = 0.9$ and $\epsilon_2 = 1.0$ for $Re_D = 500$, and $\epsilon_2 = 0$, $\epsilon_2 = 0.85$, $\epsilon_2 = 0.9$ and $\epsilon_2 = 1.0$ for $Re_D = 10^4$ ere performed. Figure 8 plots the power gain coefficient η as a function of ϵ_2. Note that the value of η at $Re = 10^4$ has been enlarged by three times in order to show the variation more clearly. We observe that the minimum of η for $Re_D = 500$ is around $\epsilon_2 = 0.75$, and it is $\epsilon_2 = 0.9$ for $Re_D = 10^4$.

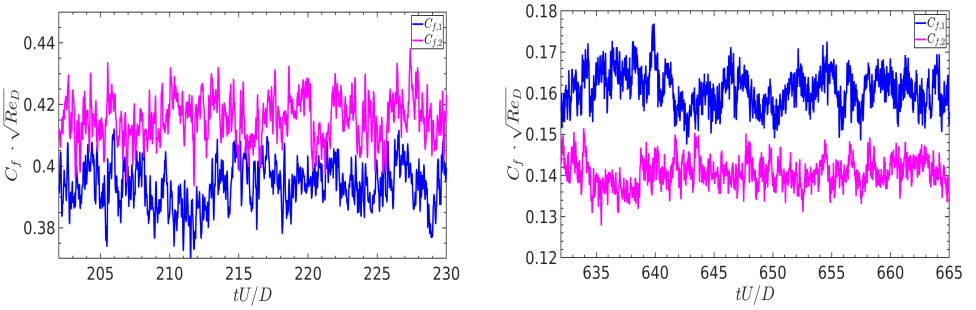

(a) $Re_D = 10^4$. (b) $Re_D = 1.4 \times 10^5$.

Figure 7: Time series of frictional coefficient (C_f) on the the control cylinders at $Re_D = 10^4$ and $Re_D = 1.4 \times 10^5$, $\epsilon_1 = 1$, $\epsilon_2 = 1$, $\epsilon_{\text{max=3.66}}$.

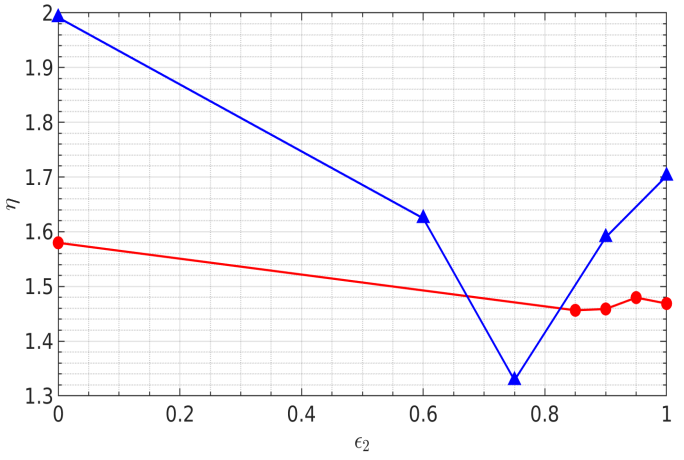

Figure 8: Power gain coefficient (η) varies with ϵ: blue one, $Re_D = 500$; red one, $Re_D = 10^4$. Note that at $Re_D = 10^4$, the value of η has been enlarged by three times. $\epsilon_{\text{max}} = 3.66$.

Appendix B. Validation of simulation of cylinder flow at high Re_D

In order to validate the numerical method (spectral element plus entropy–viscosity), large-eddy simulations of flow past a cylinder at $Re_D = 1.4 \times 10^5$ have been performed. The computational domain has a size of $[-12\,D, 16\,D] \times [-10\,D, 10\,D]$ in streamwise (x) and crossflow (y) directions, respectively. The domain is partitioned into 2 044 quadrilateral elements. The size of elements around the cylinder in the radial direction is $0.0016\,D$ in order to resolve the boundary layer. The domain size in the spanwise (z) direction is $3D$. Uniform inflow velocity is prescribed at the inflow boundary, homogeneous Neumann boundary condition for velocity and zero pressure is imposed at the outflow boundary, and wall boundary condition is imposed at cylinder surface and periodic boundary condition is assumed at all other boundaries. In particular, two simulations on different resolution are performed: LES^1, 3$^{\text{rd}}$ order spectral-element, 120 Fourier planes, $\Delta t = 1.5 \times 10^{-4}$; LES^2, 4$^{\text{th}}$ order spectral-element and 160 Fourier planes, $\Delta t = 1.0 \times 10^{-4}$.

Table 1 presents the statistical values of $\overline{C_D}$, $\overline{C_L}$, St, L_r and ϕ_s from the simulation at $Re_D = 1.4 \times 10^5$. We observe that the simulation results agree with the values obtained from literature very well, and the results are not sensitive to the mesh resolution. A further validation with the

Table 1: Sensitivity study of the simulation result to the mesh resolution: flow past a single circular cylinder at $Re_D = 1.4 \times 10^5$. $\overline{C_D}$ is the mean drag coefficient, $\overline{C_L}$ is the r.m.s. value of the lift coefficient, St is the Strouhal number, L_r is the length of the recirculation bubble and ϕ_s is the separation angle. The (Breuer 2000) LES is case D2. LES^1 and LES^2 corresponds to the mesh resolution 1 and 2, respectively.

Study	$\overline{C_D}$	$\overline{C_L}$	St	L_r	ϕ_s
Present LES ^{1}	0.95	0.63	0.22	0.69	93
Present LES ^{2}	1.13	0.49	0.21	0.74	94
(Breuer 2000) LES	1.29	-	0.203	0.46	92.59
(Braza *et al.* 2006) Experiment	-	-	0.21	0.78	

experimental measurement is shown in figure 9, which plots the mean local $\overline{C_p}$ and $\overline{C_f}$. Again, the simulation results agree with experimental measurement very well. Figure 10 exhibits the comparison between present LES and the experimental measurement by Cantwell & Coles (1983). It could be observed that the LES results of the mean stremwise velocity $\frac{\overline{u}}{U_\infty}$ along horizontal line $y = 0$ and vertical line $x/D = 1$ are in good agreement with the experiments. Figure 11 shows the streamlines and contours of the mean velocity and Reynolds stress in the near wake. The results shown in the figures agree with Fig.5 and Fig. 6 of Braza *et al.* (2006) well.

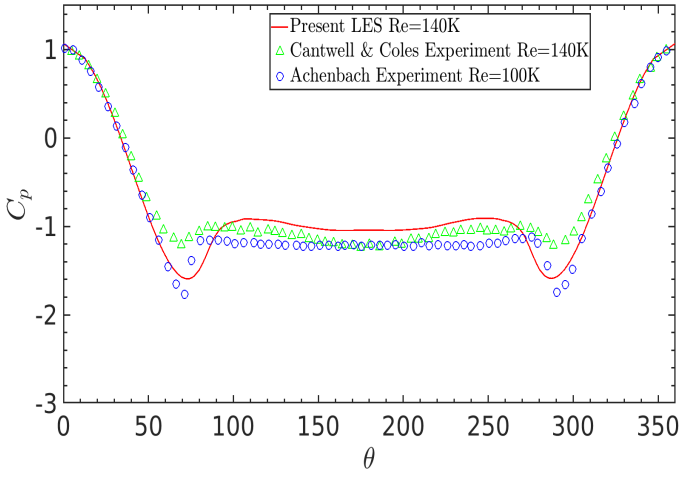

(a)

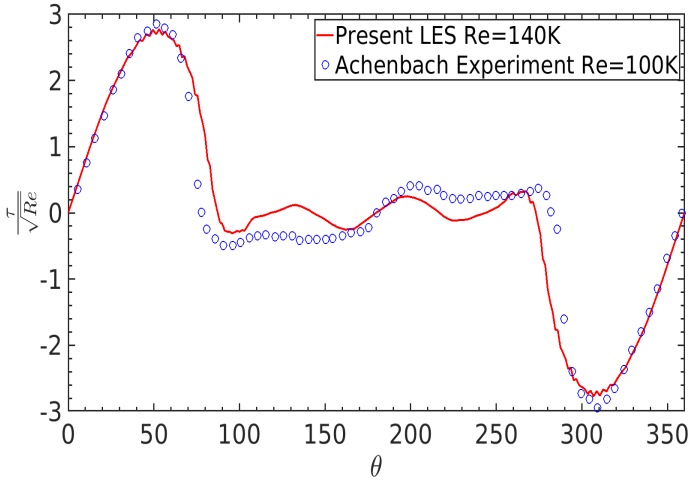

(b)

Figure 9: Local pressure and skin friction coefficient at $Re_D = 1.4 \times 10^5$, comparison with the literature. Note that "Present LES" is from the simulation using mesh LES[2],"Cantwell & Coles Experiment" refers to the experiment by Cantwell & Coles (1983), "Achenbach Experiment" refers to the experiment by Achenbach (1968).

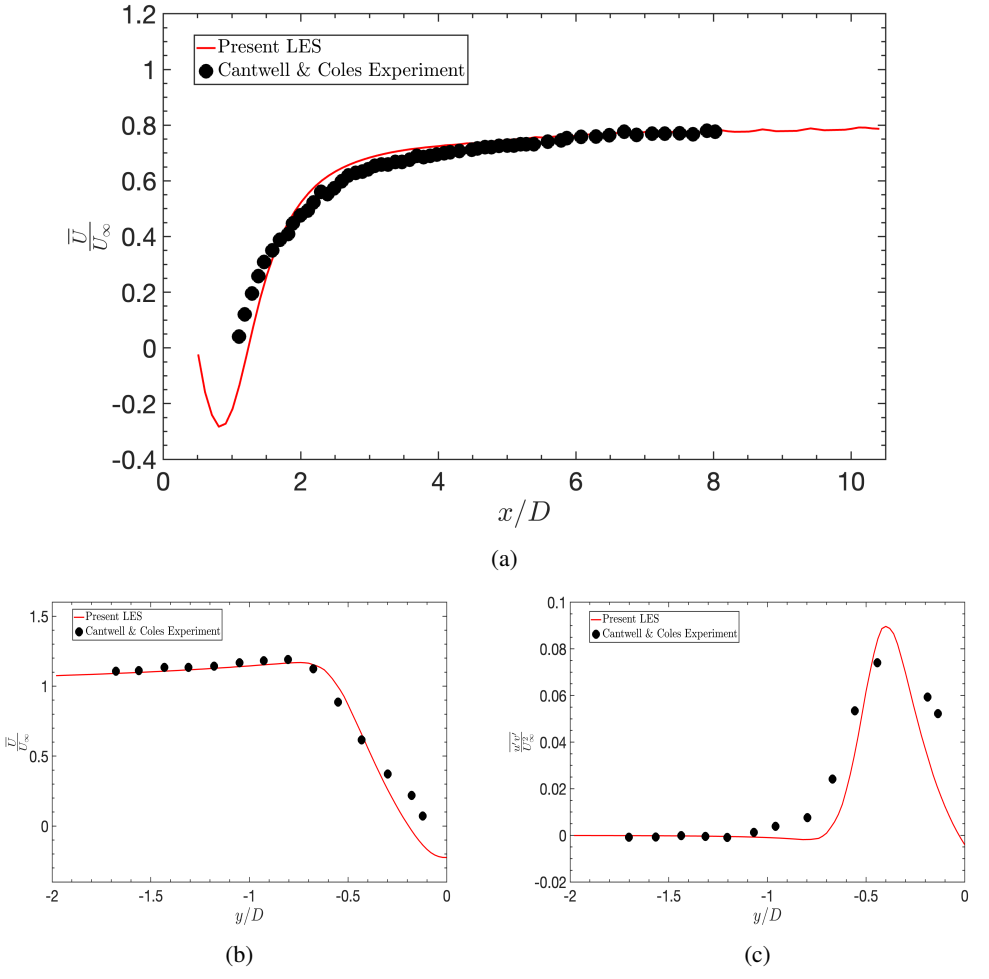

Figure 10: Validation of the LES: (a) Mean center-line velocity $\frac{\overline{u}}{U_\infty}$; (b) mean velocity $\frac{\overline{u}}{U_\infty}$ at $\frac{x}{D} = 1$; (c) mean turbulent shear stress $\frac{\overline{u'v'}}{U_\infty^2}$ at $\frac{x}{D} = 1$. Note that "Present LES" is from the simulation using mesh LES^2, "Cantwell & Coles Experiment" refers to the experiment by Cantwell & Coles (1983).

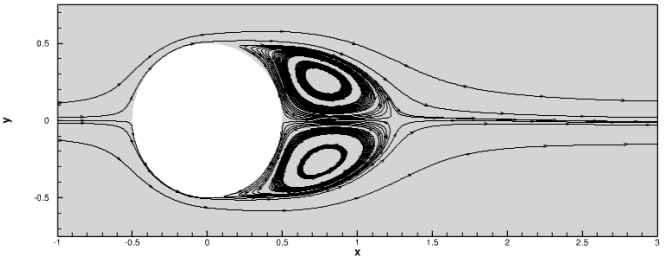

(a) streamlines

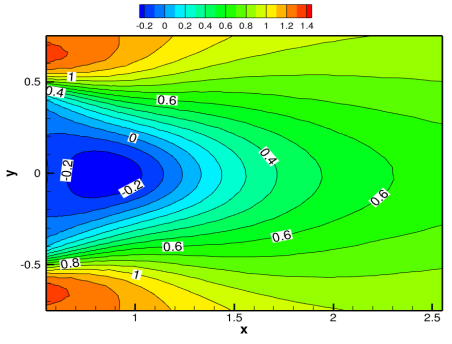

(b) $\overline{u}$

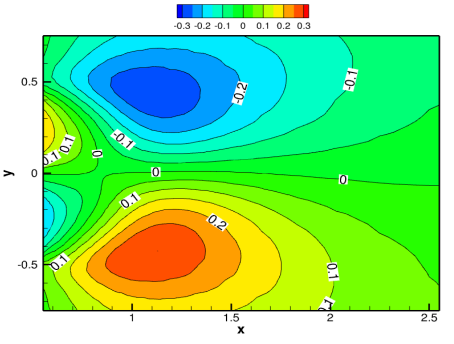

(c) $\overline{v}$

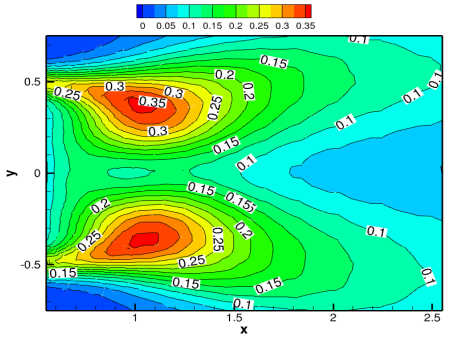

(d) $\overline{uu}$

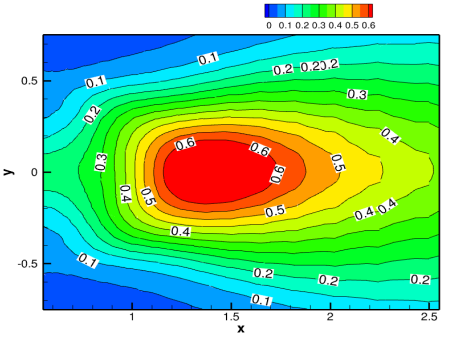

(e) $\overline{vv}$

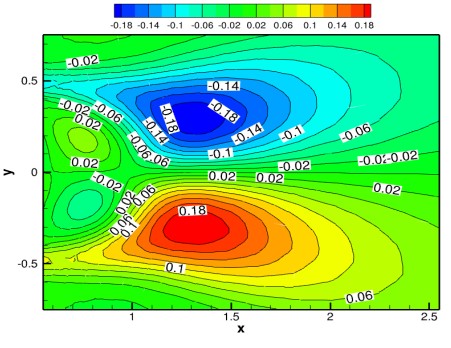

(f) $\overline{uv}$

Figure 11: Validation of the LES: mean velocity and Reynolds stress field. The results is from the simulation using mesh resolution LES^2

REFERENCES

Achenbach, E. 1968 Distribution of local pressure and skin friction around a circular cylinder in cross-flow up to re = 5 × 106. *Journal of Fluid Mechanics* **34** (4), 625–639.

Bae, J. & Koumoutsakos, P. 2022 Scientific multi-agent reinforcement learning for wall-models of turbulent flows. *Nature Communications* **13**, 1443.

Braza, M., Perrin, R. & Hoarau, Y. 2006 Turbulence properties in the cylinder wake at high reynolds numbers. *Journal of Fluids and Structures* **22** (6), 757–771, "Bluff Body Wakes and Vortex-Induced Vibrations (BBVIV-4).

Breuer, Michael 2000 A challenging test case for large eddy simulation: high reynolds number circular cylinder flow. *International Journal of Heat and Fluid Flow* **21** (5), 648–654, turbulence and Shear Flow Phenomena 1.

Bucci, M., Semeraro, O., Allauzen, A., Wisniewski, G., Cordier, L. & Mathelin, L. 2019 Control of chaotic systems by deep reinforcement learning. *Proceedings of the Royal Society A: Mathematical, Physical and Engineering Sciences* **475** (2231), 20190351.

Cantwell, Brian & Coles, Donald 1983 An experimental study of entrainment and transport in the turbulent near wake of a circular cylinder. *Journal of Fluid Mechanics* **136**, 321–374.

Cheng, W., Pullin, D., Samtaney, R., Zhang, W. & Gao, W. 2017 Large-eddy simulation of flow over a cylinder with re_D from 3.9×10^3 to 8.5×10^5: a skin-friction perspective. *Journal of Fluid Mechanics* **820**, 121–158.

Colabrese, S., Gustavsson, K., Celani, A. & Biferale, L. 2017 Flow navigation by smart microswimmers via reinforcement learning. *Physical Review Letters* **118** (15), 158004.

Dong, S., Karniadakis, G.E., Ekmekci, A. & Rockwell, D. 2006 A combined direct numerical simulation–particle image velocimetry study of the turbulent near wake. *Journal of Fluid Mechanics* **569**, 185–207.

Fan, D., Yang, L., Wang, Z., Triantafyllou, M. & Karniadaki, s G.E. 2020 Reinforcement learning for bluff body active flow control in experiments and simulations. *Proceedings of the National Academy of Sciences* **117** (42), 26091–26098.

Fujimoto, S., Hoof, V. & Meger, D. 2018 Addressing function approximation error in actor-critic methods. In *International Conference on Machine Learning*, pp. 1582–1591.

Gazzola, M., Hejazialhosseini, B. & Koumoutsakos, P. 2014 Reinforcement learning and wavelet adapted vortex methods for simulations of self-propelled swimmers. *SIAM Journal on Scientific Computing* **36** (3), B622–B639.

Guermond, J-L., Pasquetti, R. & Popov, B. 2011*a* Entropy viscosity method for nonlinear conservation law. *Journal of Computational Physics* **230** (11), 4248–4267.

Guermond, J-L., Pasquetti, R. & Popov, B. 2011*b* From suitable weak solutions to entropy viscosity. *Journal of Scientific Computing* **49** (1), 35–50.

Karniadakis, G.E. & Sherwin, S. 2005 *Spectral/hp Element Methods for Computational Fluid Dynamics, 2nd edition*. Oxford,UK: Oxford University Press.

Kirkpatrick, J., Pascanu, R., Rabinowitz, N., Veness, J., Desjardins, G., Rusu, A., Milan, K., Quan, J., Ramalho, T., Grabska-Barwinska, A., Hassabis, D., Clopath, C., Kumaran, D. & Hadsell, R. 2017 Overcoming catastrophic forgetting in neural networks. *Proceedings of the National Academy of Sciences* **114** (13), 3521–3526.

Ma, P., Tian, Y., Pan, Z., Ren, B. & Manocha, D. 2018 Fluid directed rigid body control using deep reinforcement learning. *ACM Transactions on Graphics (TOG)* **37** (4), 96.

Morkovin, M. 1964 Flow around circular cylinders-a kaleidoscope of challenging fluid phenomena. In *Proceedings of ASME Symposium on Fully Separated Flows*, pp. 102–118.

Novati, G., Mahadevan, L. & Koumoutsakos, P. 2019 Controlled gliding and perching through deep-reinforcement-learning. *Physical Review Fluids* **4** (9), 093902.

Rabault, J., Kuchta, M., Jensen, A., Réglade, U. & Cerardi, N. 2019 Artificial neural networks trained through deep reinforcement learning discover control strategies for active flow control. *Journal of Fluid Mechanics* **865**, 281–302.

Reddy, G., Celani, A., Sejnowski, T. & Vergassola, M. 2016 Learning to soar in turbulent environments. *Proceedings of the National Academy of Sciences* **113** (33), E4877–E4884.

Ren, F., Rabault, J. & Tang, H. 2021 Applying deep reinforcement learning to active flow control in weakly turbulent conditions. *Physics of Fluids* **33** (3), 037121.

Verma, S., Novati, G. & Koumoutsakos, P. 2018 Efficient collective swimming by harnessing vortices

through deep reinforcement learning. *Proceedings of the National Academy of Sciences* **115** (23), 5849–5854.

Viquerat, J., Rabault, J., Kuhnle, A., Ghraieb, H., Larcher, A. & Hachem, E. 2021 Direct shape optimization through deep reinforcement learning. *Journal of Computational Physics* **428**, 110080.

Wang, Z., Triantafyllou, M. S., Constantinides, Y. & Karniadakis, G.E. 2018 A spectral-element/fourier smoothed profile method for large-eddy simulations of complex viv problems. *Computers and Fluids* **172**, 84–96.

Wang, Z., Triantafyllou, M. S., Constantinides, Y. & Karniadakis, G.E. 2019 An entropy-viscosity large eddy simulation study of turbulent flow in a flexible pipe. *Journal of Fluid Mechanics* **859**, 691–730.